Title: Silicon Electrodeposition in a Water-soluble KF–KCl Molten Salt: Effects of Temperature and Current Density

Author Names: Kouji YASUDA,[1,2,*,z] Kazumi SAEKI,[1] Tomonori KATO,[3] Rika HAGIWARA,[1,*] and Toshiyuki NOHIRA[3,*,z]

Affiliation(s): [1] Department of Fundamental Energy Science, Graduate School of Energy Science, Kyoto University, Yoshida-honmachi, Sakyo-ku, Kyoto 606-8501, Japan.

[2] Agency for Health, Safety and Environment, Kyoto University, Yoshida-honmachi, Sakyo-ku, Kyoto 606-8501, Japan.

[3] Institute of Advanced Energy, Kyoto University, Gokasho, Uji 611-0011, Japan.

* Electrochemistry Society Active Member

[z]Corresponding Author E-mail Addresses: yasuda.kouji.3v@kyoto-u.ac.jp (K. Yasuda); nohira.toshiyuki.8r@kyoto-u.ac.jp (T. Nohira)

Abstract Text [200 Words or Less]

The effects of temperature and current density on the electrodeposition of Si films in molten KF–KCl–K_2SiF_6 were investigated at 923–1073 K. The peak current density of Si deposition in cyclic voltammetry increased as the temperature rose. The diffusion coefficient of Si (IV) ions measured by chronoamperometry increased through a rise in temperature. The activation energy for the diffusion of Si (IV) ions, 28.0 kJ mol^{-1}, agreed with that for the viscosity of KF and KCl. The crystallinity of the Si films prepared by galvanostatic electrolysis on Ag substrates was measured based on electron backscatter diffraction. The largest crystallite size in the deposited Si increased with the deposition temperature, from a submicron size at 923 K, to several tens of microns at 1073 K. Moreover, even at the same temperature of 1073 K, larger crystallite sizes were observed for the Si deposit at 100 mA cm^{-2} as compared with that at 300 mA cm^{-2}, which was explained based on the crystallization rate of Si.

Introduction

One significant item to be noted in the energy field is a drastic increase in the number of photovoltaic (PV) installations. The annual installation of PV cells exceeded 100 GW globally in 2017 [1, 2]. There is no doubt that PV power generation will be one of the major energy sources in the future. Crystalline Si solar cells are expected to continuously dominate the share of production of solar cell types owing to their high efficiency, excellent stability, non-toxicity, and abundant natural resource. However, the low productivity of the Siemens process and the considerable kerf loss in the slicing step are the main drawbacks in the current production method of the Si substrates used for PV cells. Therefore, the development of an alternative process for the efficient manufacturing of crystalline Si substrates is necessary to enable a significant improvement in the PV production efficiency.

The direct formation of Si films on inexpensive substrates has been proposed and investigated as an alternative method for producing polycrystalline Si solar cells. Electrodeposition of crystalline Si has been reported in high-temperature molten salts [3–12]; whereas it has hardly been achieved in organic solvents and ionic liquids. Compact and smooth Si films have been obtained in all-fluoride molten salts such as LiF–KF and LiF–NaF–KF [3, 4, 6–8]. The major problem in the use of all-fluoride molten salts is the low solubility of LiF in water. The salt adhered to deposited Si is difficult to remove through water washing [7, 12]. A lack of high-purity and low-cost Si sources is an additional problem.

Based on this background, we proposed and investigated a new electrodeposition process for the formation of crystalline Si films, utilizing a water-soluble KF–KCl molten salt as an

electrolyte, and gaseous $SiCl_4$ as a Si source [13–16]. Through this process, gaseous $SiCl_4$ is dissolved into a molten salt to form Si (IV) complex ions.

$SiCl_4$ dissolution: $SiCl_4\ (g) + 6\ F^- \rightarrow SiF_6^{2-} + 4\ Cl^-$ (1)

It should be noted that $SiCl_4$ is inexpensive and easily purified. Si films are electrodeposited onto the cathode of an appropriate substrate, and Cl_2 gas is evolved at a carbon anode.

Cathodic reaction: $SiF_6^{2-} + 4\ e^- \rightarrow Si\ (s) + 6\ F^-$ (2)

Anodic reaction: $4\ Cl^- \rightarrow 2\ Cl_2\ (g) + 4\ e^-$ (3)

The composition of molten salt remains unchanged during operation, as can be seen from the following total reaction.

Total reaction: $SiCl_4\ (g) \rightarrow Si\ (s) + 2\ Cl_2\ (g)$ (4)

Moreover, since the evolved Cl_2 gas can be reused for the production of $SiCl_4$, it is possible to construct a closed-cycle production system. One advantage of our proposed process is the high solubility of the solidified KF–KCl salt in water (the solubility of KF and KCl is 101.6 and

35.9 g, respectively, per 100 g of H_2O at 298 K) as compared to other fluoride salts (the solubility of LiF, NaF, MgF_2, and CaF_2 is 0.13, 4.15, 0.13, and 0.0016 g, respectively, per 100 g of H_2O at 298 K) [17]. Thus, the salt adhering to a Si deposit is easily removed by washing with water. In spite of the high solubility to water, this molten salt has a high fluoride ion concentration, which is essential in obtaining compact and smooth Si films. We previously investigated the electrodeposition of Si from Si(IV) complex ions on a Ag electrode in a molten KF–KCl–K_2SiF_6 system at 923 K [13–15]. Si films electrodeposited at a current density of 50–200 mA cm^{-2} in the molten salt containing 2.0–3.5 mol% K_2SiF_6 exhibited adherent, compact, and smooth characteristics. The residual salt on the deposited Si was easily removed by simply soaking the film in water. A cathodic reaction was found to proceed through an E_qE_r (quasi-reversible–reversible electron transfer reaction) mechanism, and the diffusion coefficient of the Si(IV) ions was calculated to be 3.2×10^{-5} cm^2 s^{-1} at 923 K [14].

The present study aimed at investigating the formation of adherent, compact, and smooth Si films with higher crystallinity in molten KF–KCl by elevating the operation temperature from 923 to 1073 K. High crystallinity is necessary to achieve high conversion efficiency in photovoltaics. The electrochemical behavior of Si (IV) ions was measured using cyclic voltammetry and chronoamperometry at 923, 973, 1023, and 1073 K. The electrodeposits obtained by galvanostatic electrolysis were analyzed using cross-sectional scanning electron microscopy, X-ray diffraction, and electron backscatter diffraction. The effects of the temperature and current density on the crystallinity and preferred orientation are discussed herein.

Experimental

The experiment setup used was described elsewhere [15]. The electrochemical experiments were conducted in a dry Ar glove box at 923–1073 K. Reagent-grade KF and KCl were mixed to the eutectic composition (KF:KCl = 45:55 mol%, melting point = 878 K [18]) and loaded into a graphite crucible. The crucible was placed at the bottom of a stainless-steel vessel in an airtight Kanthal container and dried under a vacuum at 673 K for 24 h. A Ag wire (Nilaco Corp., >99.99%, diameter = 1.0 mm), a Ag flag (Nilaco Corp., 99.98%, diameter = 2.0 mm, thickness = 0.1 mm [14]), and a Ag plate (Nilaco Corp., 99.98%, thickness = 0.2 mm) were used as the working electrodes. A glassy carbon rod (Tokai Carbon Co., Ltd., diameter = 3.0 mm) was used as the counter electrode. A Pt wire (Nilaco Corp., >99.98%, diameter = 1.0 mm) and a Si plate (p-type, resistivity = 9–12 Ω·cm, *ca*. 5 × 5 × 0.73 mm) were employed as the quasi-reference electrode and reference electrode, respectively. Since the consumption of Si(IV) ions during the Si electrodeposition experiments was less than 0.1% of the added Si ions, the Si electrode showed a quite stable potential of Si(IV)/Si(0). The potential of the reference electrode was calibrated with reference to the dynamic K^+/K potential [14]. Galvanostatic electrolysis was conducted on the Ag substrates. The electrolyzed samples were washed in hot distilled water at 333 K for 24 h to remove the salt adhered onto the deposits, and dried under a vacuum for 12 h. The samples were analyzed using scanning electron microscopy (SEM, Keyence Corp., VE-8800) and X-ray diffraction (XRD; Rigaku Corp., Ultima IV, Cu-Kα line). For the cross-sectional SEM observations, the samples were embedded in an acrylic resin and fabricated using a cross-section polisher with an Ar ion beam. The crystallinity was measured by field-emission

scanning electron microscope (FE-SEM; ZEISS, SUPRA35VP, or JEOL, JSM 7800F TSL) and electron backscatter diffraction (EBSD, ZEISS, SUPRA35VP + OIM5.31, SUPRA35VP + OIM6.2, or JEOL, JSM 7800F TSL + OIM7.1).

Results and Discussion

Electrochemical measurement

The electrochemical behavior of Si (IV) ions was investigated by cyclic voltammetry. A Ag flag electrode was used because there is no intermetallic phase between Ag and Si [19]. Figure 1 shows the cyclic voltammograms obtained at 923 K and 1073 K in molten KF–KCl–K_2SiF_6 (0.10 mol%). Reduction currents are observed from *ca.* 0.75 V vs. K^+/K at both temperatures. After the reversal of the sweep direction, two anodic waves, a shoulder and a peak, are observed from *ca.* 0.75 V at each temperature. These redox currents correspond to the cathodic deposition of Si and the anodic dissolution of Si [13–15]. The appearance of the oxidation shoulder probably reflects a formation of intermediate products in the dissolution reaction, which needs to be clarified in the future.

Figure 2(a) shows the cyclic voltammograms at different scan rates of 0.2, 0.5, 1.0, and 2.0 V s^{-1} at 1073 K. The cathodic peak potential apparently shifts toward a negative value with an increase in the scan rate, indicating that the electrochemical reaction is either an irreversible process or a quasi-reversible process.

To clarify whether the electrochemical reaction is irreversible or quasi-reversible, the relationship between the peak potential and the logarithm of the scan rate was investigated. The cathodic peal potential, E_p, for an irreversible process is given by Eq. 5:

$$E_p - E^{\circ\prime} = -0.780\frac{RT}{\alpha nF} - \frac{RT}{\alpha nF}\ln[\left(\frac{\alpha nFD_O v}{RT}\right)^{\frac{1}{2}}\frac{1}{k^\circ}] \quad (5)$$

where E^{o}' is the formal potential, R is the universal gas constant, T is the absolute temperature, α is the transfer coefficient, n is the number of electrons involved in the charge-transfer step, F is the Faraday constant, D_o is the diffusion coefficient of the ions, v is the scan rate, and $k°$ is the charge-transfer rate constant [20, 21]. The values of E_p in Fig. 2(a) are plotted against $\ln v$ in Fig. 2(b). A linear relationship between E_p and $\ln v$ is observed, indicating that the electrochemical reaction is an irreversible process at 1073 K. The transfer coefficient derived from the slope is 0.56. Here, the volume concentration of ions in the electrolyte, c_o, is calculated to be 2.45×10^{-5} mol cm^{-3} for the melt containing 0.1mol% K_2SiF_6 at 1073 K using the estimated density of the KF–KCl melt from the reported values at 50:50 mol% and 63:37 mol% [22]. The transfer coefficient was also determined from E_p and half-wave potential, $E_{p/2}$, according to the following equation for an irreversible system,

$$E_p - E_{p/2} = -1.857\frac{RT}{\alpha nF} \quad (6).$$

The value of α was calculated to be 0.56 both at v = 0.2 and 2.0 V s^{-1}, which agrees with the analysis by Fig. 2(b).

*** Fig. 1 ***

*** Fig. 2 ***

The diffusion coefficient of Si(IV) ions was evaluated from chronoamperometry in molten KF–KCl–K_2SiF_6 (0.10 mol%) at different temperatures of 923–1073 K. For the evaluation, the potential was set to the mass-transfer-limited region of 0.55 V, which was more negative than the peak potential of Si deposition for the cyclic voltammogram at a scan rate of 0.5 V s^{-1}. When the rate-determining step is the diffusion of ions, the current-time response follows a Cottrell equation. The current, I, is proportional to the reciprocal of the square root of time, t [20, 23]:

$$I = -\frac{nFAD_{\mathrm{O}}^{1/2}c_{\mathrm{O}}}{\pi^{1/2}t^{1/2}} . \quad (7)$$

Here, A is the electrode area, and c_o is the concentration of ions in the electrolyte. When the current density, $i = I/A$, is plotted against the reciprocal of the square root of time, D_o can be calculated from the slope. Figure 3 shows i–$t^{-1/2}$ plots for the chronoamperograms measured at 0.55 V ($2<t^{-1/2}<5$) at temperatures of 923, 973, 1023, and 1073 K. Because a proportional relationship is observed at all temperatures, D_o is calculated from the slope. The diffusion coefficients are calculated as 5.9×10^{-5} cm^2 s^{-1} at 923 K, and 10.0×10^{-5} cm^2 s^{-1} at 1073 K. Table 1 summarizes all values calculated at different temperatures, as well as the previously reported values [14, 24]. The value at 923 K in the present study is close to that obtained by Boiko *et al.* when using chronoamperometry (5.6×10^{-5} cm^2 s^{-1} at 923 K) [24]. The results of our previous study [14] (3.2×10^{-5} cm^2 s^{-1} at 923 K) might have underestimated the value.

To analyze the temperature dependence of D_o, Arrhenius plots were created, as shown in Figure 4. When the diffusion is governed by an Arrhenius-type behavior, the diffusion

coefficient changes according to Eq. (8):

$$D_o = D_o' \exp\left(\frac{-W}{RT}\right). \quad (8)$$

Here, D_o' is a constant and W is the activation energy. From the slope in Fig. 4, the activation energy is calculated as 28.0 kJ mol^{-1}, and D_o is expressed as a function of temperature.

$$D_o = 2.23\times10^{-3}\times10^{-1.46\times10^3/T} \ (cm^2\ s^{-1}) \quad (9)$$

In general, the relationship between the diffusion coefficient and viscosity, v, is known as the Stokes-Einstein equation,

$$vD = \frac{kT}{6\pi a} \quad (10)$$

where k is the Boltzmann constant, and a is the radius. From Eqs. (8) and (10), the following equation is obtained:

$$\ln\frac{v}{T} = \ln\frac{k}{6D'a} + \left(\frac{W}{RT}\right) \quad (11)$$

Although the temperature dependence of viscosity for the KF–KCl eutectic melt has yet to be reported, those for both a single KF melt and a single KCl melt have been documented [22].

From the reported values, Arrhenius plots of vT^{-1} have been created, from which the activation energies for KF and KCl were calculated to be 32.1 and 33.3 kJ mol^{-1}, respectively. These values are close to the activation energy of D_o, namely, 28.0 kJ mol^{-1}, indicating that the diffusion of Si (IV) ions has a relation with the viscosity in accordance with the Stokes-Einstein equation.

*** Fig. 3 ***

*** Fig. 4 ***

Crystallinity of Si films

Effect of temperature: The effects of temperature on the crystallinity and preferred orientation were investigated for the Si deposits. The samples were prepared by galvanostatic electrolysis on Ag substrates. According to a series of deposition experiments and cross-sectional SEM observations, the conditions to deposit relatively compact and smooth Si layers on a Ag substrate have been determined at 1073 K, namely, the concentration range of K_2SiF_6 is 2.0–3.5 mol%, and the current density range is 100–300 mA cm^{-2}. Concerning the optimum deposition condition at 923 K, our previous study revealed a K_2SiF_6 concentration of 2.0–3.5 mol% and a current density of 50–200 mA cm^{-2} [15].

Figure 5 compares the XRD patterns of the deposits obtained by a galvanostatic electrolysis of Ag plate electrodes at 100 mA cm^{-2} in molten KF–KCl–K_2SiF_6 (2.0 mol%) at (a) 923 K and (b) 1073 K. Both samples were confirmed to be crystalline Si. The crystallite size was evaluated according to the Scherrer equation [25] from the full maximum at

223 half-maximum (FMHM) for the 220 plane.

224

$$D = \frac{K\lambda}{\beta \cos\theta} \quad (12)$$

225

226

227 Here, D is the crystallite size, K is the Sherrer constant (0.94), λ is the wavelength (0.15418
228 nm), β is the FMHM, and θ is the Bragg angle. The crystallite sizes obtained from Eq. (12)
229 were 47 nm and 136 nm at 923 K and 1073 K, respectively. Although the Scherrer equation is
230 only applicable for a nano-scaled crystal of smaller than 100 nm [25], the results indicated
231 that the crystallinity was higher at 1073 K. In addition, a highly preferred orientation toward
232 the <110> direction is observed at 1073 K.

233

234 *** Fig. 5 ***

235

236 The crystallinity of the Si deposits was further evaluated by cross-sectional FE-SEM and
237 EBSD. Figure 6(a-1) shows a cross-sectional FE-SEM image of the sample obtained by
238 galvanostatic electrolysis at 155 mA cm^{-2} for 20 min in molten KF–KCl–K_2SiF_6 (2.0 mol%)
239 at 923 K. The formation of an adherent, compact, and smooth Si film with a thickness of 50
240 μm is observed on a Ag substrate. The crystal grain map from an EBSD analysis of the Si
241 deposit is shown in Fig. 6(a-2). In the map, a crystal orientation is indicated by color, as
242 shown in the inverse pole figure, and the crystallite size, based on the area, is indicated using
243 a particular color. Very fine grains and a crystal grain boundary are indicated in black. Figure
244 6(a-2) clarifies that most of the crystals are very fine, whereas only a part of the deposit is

245 composed of crystal grains of larger than 1 μm. The crystal growth of Si is considered to be
246 slow at 923 K.

247 A cross-sectional FE-SEM image and EBSD analytical results for the deposit at 1073 K
248 are shown in Figs. 6(b-1) and 6(b-2), respectively. With the exception of temperature, the
249 electrolysis conditions were the same as those at 923 K. The crystal grain map shows the
250 columnar growth of Si crystals toward the vertical direction of the substrate. The crystallite is
251 3 μm in width and 20 μm in length, which is larger than those deposited at 923 K. The higher
252 crystallinity with columnar Si crystals at 1073 K is explained based on the crystallization rate.
253 Table 2 compares the reported crystallization [26] and theoretical deposition rates at 155 mA
254 cm^{-2}. Because the crystallization rate is slower than the deposition rate at 923 K, only fine Si
255 grains were deposited. In contrast, large columnar Si crystals grew at 1073 K because the
256 crystallization rate is larger than the deposition rate.

257

258 *** Fig. 6 ***

259

260 *Effects of current density*

261 To obtain Si films with high crystallinity, the effects of the current density were
262 investigated at 1073 K. The samples were prepared on Ag substrates at cathodic current
263 densities of 100 mA cm^{-2} and 300 mA cm^{-2} with the same electric charge of 270 C cm^{-2}. As
264 shown in Fig. 7, only peaks attributed to crystalline Si are observed by XRD. An estimation
265 of the crystallite size using the Scherrer equation cannot be applied owing to the presence of
266 sharp peaks, indicating a crystallite size of larger than 100 nm.

Then, the crystallinity was evaluated by an EBSD analysis for the cross-sections, as shown in Fig. 8. At 100 mA cm^{-2}, a flat and compact Si film with a thickness of 35 μm is deposited onto the Ag substrate (Fig. 8(a-1)). The crystal grain map from the EBSD analysis of the Si deposit is shown in Fig. 8(a-2). The crystallite size is smaller within the vicinity of the substrate, and larger at the film surface. The crystal grows into a columnar structure with a size of up to 15 μm × 30 μm. These results are explained by the various orientations of the crystals during the initial deposition stage, and based on the fact that the crystals grow into preferred orientations during the later deposition stage. At 300 mA cm^{-2}, a Si film with a thickness of 15 μm is deposited at the center of the substrate (Fig. 8(b-1)). In spite of the same electric charge, the thickness at the center is smaller owing to the preferential deposition at the edges of the substrate. A crystal grain map determined from the EBSD analysis shown in Fig. 8(b-2) indicates that the size of the columnar Si crystallite reaches up to 5 μm × 15 μm. The maximum crystallite size becomes smaller with the increase in current density.

*** Fig. 7 ***

*** Fig. 8 ***

The electrodeposits were further measured by a surface EBSD analysis. The analysis was carried out for a tilted plane of the sample embedded in resin and fabricated with a cross-section polisher using an Ar ion beam, as shown in Fig. 9(a). Through this type of tilted polishing, it is possible to simultaneously analyze all depths from the innermost area to the surface. Figures 9(b) and 9(c) show the crystal grain maps of the Si deposits obtained by

galvanostatic electrolysis at 100 mA cm^{-2} and 300 mA cm^{-2}, respectively. The upper and lower areas in the images indicate the surface and substrate sides, respectively. The crystallite size is smaller in the substrate side at both current densities, which agrees with the results of the cross-sectional EBSD shown in Fig. 8. Figure 10 shows the size distribution of the crystallite size based on the results from Fig. 9. Approximately 60% of the crystallites are larger than 10 μm at 100 mA cm^{-2}, whereas more than 75% of the crystallites are smaller than 10 μm at 300 mA cm^{-2}. These results clearly show that a lower current density provides a larger crystallite size.

*** Fig. 9 ***

*** Fig. 10 ***

A surface EBSD analysis also provides information on the crystal orientation of the deposits. The crystal face parallel to the surface plane was analyzed, and the results obtained are shown with reverse pole figures. Figures 11(a) and 11(b) indicate the orientation of the surface plane for the Si deposits prepared at 100 mA cm^{-2} and 300 mA cm^{-2}, respectively. In the reverse pole figures, the red color shows the highly preferred orientation. At both current densities, the <110> direction is found to be the preferred deposition direction, which agrees with the XRD results shown in Figs. 5 and 7.

*** Fig. 11 ***

Conclusions

The electrodeposition of Si from KF–KCl–K_2SiF_6 molten salt was investigated at 923–1073 K. Based on the results of the chronoamperometry, the diffusion coefficient of Si(IV) ions was determined as a function of temperature.

$$D = 2.23\times10^{-3}\times10^{-1.46\times10^{3}/T} \quad (\mathrm{cm^2\ s^{-1}})$$

XRD and EBSD analyses revealed the crystallinity of Si films electrodeposited onto Ag substrates at current densities of 100 mA cm^{-2} and 300 mA cm^{-2} and temperatures of 923 K and 1073 K. The films had a preferred orientation toward the <110> direction vertical to the substrate. Higher-temperature electrodeposition accelerated the crystal growth during the deposition, resulting in columnar Si crystals. A larger crystallite size was obtained by galvanostatic electrolysis at a lower current density.

Acknowledgments

This study was partly supported by the Core Research for Evolutionary Science and Technology (CREST) of the Japan Science and Technology Agency (JST), and by the Zero-Emission Energy Research of the International Energy Agency, Kyoto University. The EBSD measurements were carried out at Sumitomo Electric Industries, Ltd.

References

1. Shigen Sogo System Inc., Photovoltaic Market 2017 (2018).
2. Arumu Publishing. Inc., Rare Metal News, on April 24, 2018.
3. U. Cohen and R. A. Huggins, *J. Electrochem.*, **123**, 381 (1976).
4. G. M. Rao, D. Elwell, and R. S. Feigelson, *J. Electrochem. Soc.*, **127**, 1940 (1980).
5. D. Elwell and R. S. Feigelson, *Sol. Energ. Mater.*, **6**, 123 (1982).
6. K. S. Osen, A. M. Martinez, S. Rolseth, H. Gudbrandsen, M. Juel, and G. M. Haarberg, *ECS Trans*., **33**, 429 (2010).
7. G. M. Haarberg, L. Famiyeh, A. M. Martinez, and K. S. Osen, *Electrochim. Acta*, **100**, 226 (2013).
8. G. M. Rao, D. Elwell, and R. S. Feigelson, *J. Electrochem. Soc.*, **128**, 1708 (1981).
9. D. Elwell, *J. Crystal Growth*, **52**, 741 (1981).
10. D. Elwell, *J. Appl. Electrochem.*, **18**, 15 (1988).
11. A. A. Andriiko, E. V. Panov, O. I. Boiko, B. V. Yakovlev, and O. Y. Borovik, *Rus. J. Electrochem.*, **33**, 1343 (1997).
12. J. Xu and G. M. Haarberg, *High Temp. Mater. Processes (De Gruyter)*, **32**, 97 (2013).
13. K. Maeda, K. Yasuda, T. Nohira, R. Hagiwara, and T. Homma, *ECS Transactions*, **64**(4), 285 (2014).
14. K. Maeda, K. Yasuda, T. Nohira, R. Hagiwara, and T. Homma, *J. Electrochem. Soc.*, **162**, D444 (2015).
15. K. Yasuda, K. Maeda, T. Nohira, R. Hagiwara, and T. Homma, *J. Electrochem. Soc.*, **163**, D95 (2016).
16. K. Yasuda, K. Maeda, R. Hagiwara, T. Homma, and T. Nohira, *J. Electrochem. Soc.*, **164**, D67 (2017).
17. R. Kubo, S. Nagakura, H. Iguchi, and H. Ezawa, *Rikagaku Jiten, 4th Edition*, Iwanami Shoten, Tokyo (1987).
18. L. P. Cook and H. F. McMurdie, *Phase Diagrams for Ceramists vol. VII*, p. 509, The American Ceramic Society Inc., Columbus (1989).
19. R. W. Olesinski, A. B. Gokhale, and G. J. Abbaschian, *J. Phase Equilib.*, **10**, 635 (1989).
20. A. J. Bard and L. R. Faulkner, *Electrochemical Methods: Fundamentals and Applications, 2nd Edition*, John Wiley& Sons, New York, p. 510 (2001).
21. R. S. Nicholson and I. Shain, *Anal. Chem*., **36**, 706 (1964).
22. G. J. Janz, *J. Phys. Chem. Ref. Date*, **17**, 1 (1988).
23. F. G. Cottrell, *Z. Physik. Chem*, **42**, 385 (1902).
24. O. I. Boiko, Y. K. Delimarskii, and R. V. Chernov, *Ukr. Khim. Zh*., **51**, 385 (1985).
25. B. D. Cullity, Agne Shofusha, Tokyo, *Elements of X-Ray Diffraction, 2nd edition* (2002).
26. C. Spinella, S. Lombardo, and F. Priolo, *J. Appl. Phys*., **84**, 5383 (1998).

Figure Captions

Fig. 1 Cyclic voltammograms for a Ag flag electrode in molten KF–KCl–K_2SiF_6 (0.10 mol%) at 923 K and 1073 K. Scan rate = 0.20 V s^{-1}.

Fig. 2 (a) Cyclic voltammograms for a Ag flag electrode in molten KF–KCl–K_2SiF_6 (0.10 mol%) at various scan rates at 1073 K. (b) Dependence of cathodic peak potential on the scan rate for the cyclic voltammograms measured in molten KF–KCl–K_2SiF_6 (0.10 mol%) at 1073 K.

Fig. 3 Relationship between the current density and the reciprocal of the square root of time for the chronoamperograms measured at 0.55 V ($2 < t^{-1/2} < 5$) in molten KF–KCl–K_2SiF_6 (0.10 mol%) at 923–1073 K.

Fig. 4 Arrhenius plot of diffusion coefficient of Si(IV) ions in molten KF–KCl–K_2SiF_6 within the temperature range of 923–1073 K.

Fig. 5 XRD patterns of the deposits obtained by galvanostatic electrolysis of a Ag plate electrode at 100 mA cm^{-2} in molten KF–KCl–K_2SiF_6 (2.0 mol%) at (a) 923 K and (b) 1073 K. (c) PDF data of powdery Si.

Fig. 6 (a-1)(b-1) Cross-sectional FE-SEM images and (a-2)(b-2) crystal grain maps from EBSD analysis of the Si deposit. The deposits were obtained by galvanostatic electrolysis on Ag wire electrodes at 155 mA cm^{-2} for 20 min in molten KF–KCl–K_2SiF_6 (2.0 mol%) at (a-1)(a-2) 923 K and (b-1)(b-2) 1073 K.

Fig. 7 XRD patterns of the deposits obtained by galvanostatic electrolysis of a Ag plate electrode at (a) 100 mA cm^{-2} and (b) 300 mA cm^{-2} in molten KF–KCl–K_2SiF_6 (2.0 mol%) at 1073 K. (c) PDF data of powdery Si.

Fig. 8 (a-1)(b-1) Cross-sectional SEM images and (a-2)(b-2) crystal grain maps from EBSD analysis of the Si deposit. The deposits were obtained by galvanostatic electrolysis on Ag plate electrodes (a-1)(a-2) at 100 mA cm^{-2} for 30 min and (b-1)(b-2) at 300 mA cm^{-2} for 10 min in molten KF–KCl–K_2SiF_6 (2.0 mol%) at 1073 K.

Fig. 9 (a) Schematic drawing of an observation plane for surface EBSD analysis. Crystal grain maps from EBSD analysis of the Si deposits obtained by galvanostatic electrolysis of Ag plate electrodes (b) at 100 mA cm^{-2} for 45 min and (c) at 300 mA cm^{-2} for 15 min in molten KF–KCl–K_2SiF_6 (2.0 mol%) at 1073 K.

Fig. 10 Size distribution of crystal grains for Si deposits measured using surface EBSD analysis. The deposits were prepared by the galvanostatic electrolysis of a Ag plate electrode (a) at 100 mA cm^{-2} for 45 min and (b) at 300 mA cm^{-2} for 15 min in molten KF–KCl–K_2SiF_6 (2.0 mol%) at 1073 K.

Fig. 11 Reverse pole figures from EBSD analysis of the Si deposits. The deposits were obtained by the galvanostatic electrolysis of a Ag plate electrode (a) at 100 mA cm^{-2} for 45 min and (b) at 300 mA cm^{-2} for 15 min in molten KF–KCl–K_2SiF_6 (2.0 mol%) at 1073 K.

Table 1 Diffusion coefficient of Si(IV) ions in KF–KCl–K_2SiF_6 (0.10 mol%) melt at various temperatures.

Temperature / K	Diffusion coefficient / $cm^2\ s^{-1}$	Reference
923	5.9×10^{-5}	This study
973	7.1×10^{-5}	
1023	8.0×10^{-5}	
1073	10.0×10^{-5}	
933	5.6×10^{-5}	[24]
923	3.2×10^{-5}	[14]

Table 2 Comparison of crystallization rate of Si with theoretical deposition rate.

Temperature / K	Crystallization rate [26] / μm s^{-1}	Theoretical deposition rate (at 155 mA cm^{-2}) / μm s^{-1}
923	3×10^{-3}	4.8×10^{-2}
1073	2×10^{-1}	4.8×10^{-2}

Figures

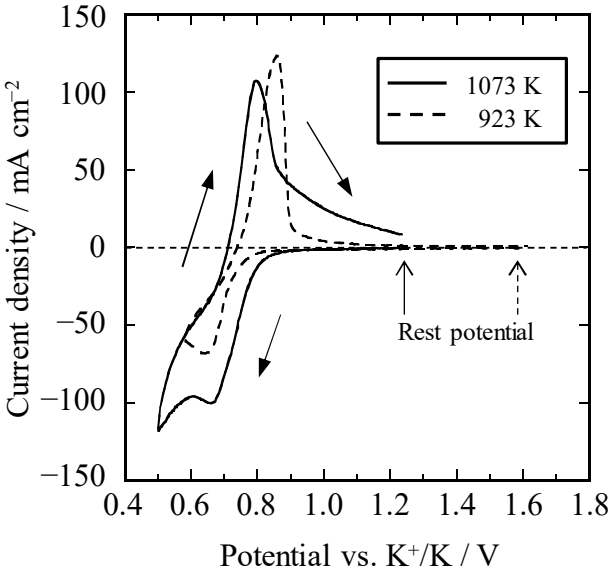

Fig. 1

(a)

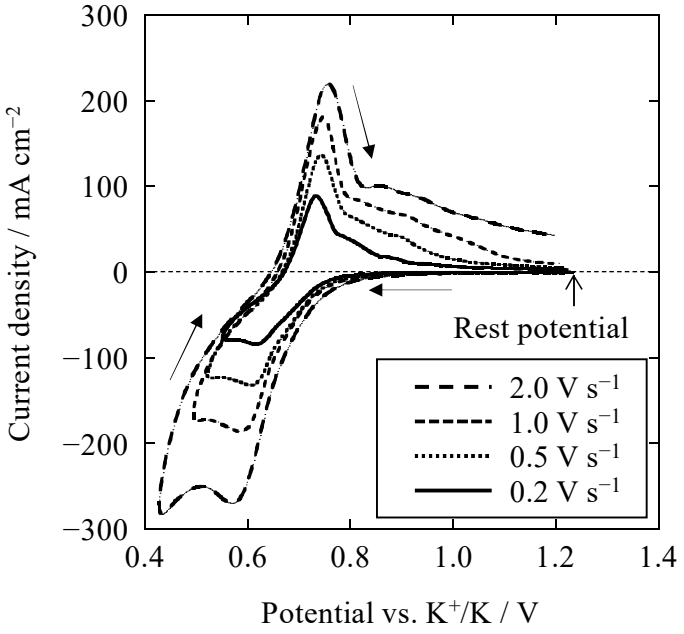
300
200
100
0
−100
−200
−300
0.4
0.6
0.8
1.0
1.2
1.4
Current density / mA cm−2
Potential vs. K+/K / V
Rest potential
2.0 V s−1
1.0 V s−1
0.5 V s−1
0.2 V s−1

(b)

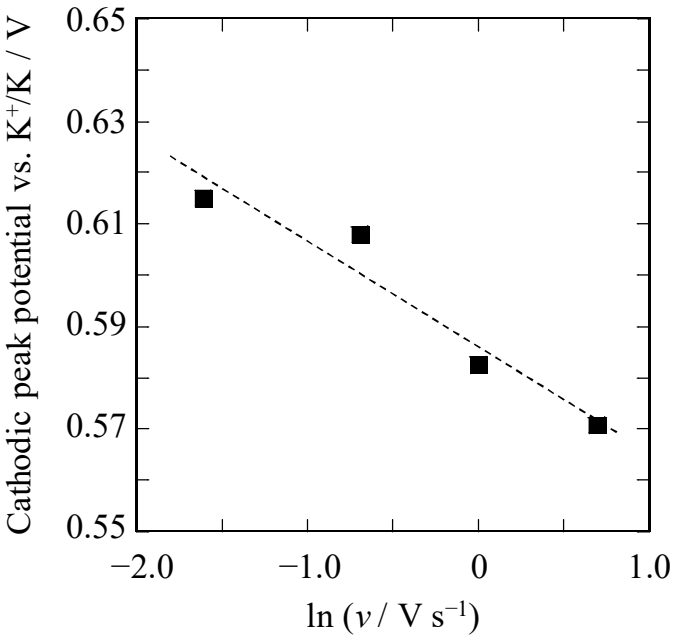
0.65
0.63
0.61
0.59
0.57
0.55
−2.0
−1.0
0
1.0
Cathodic peak potential vs. K+/K / V
ln (v / V s−1)

Fig. 2

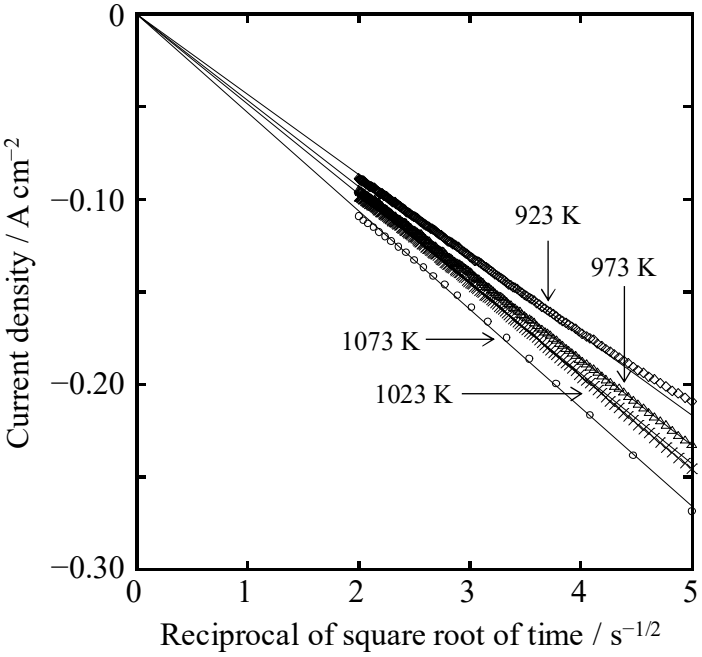
0
−0.10
−0.20
−0.30
0
1
2
3
4
5
Current density / A cm^{-2}
Reciprocal of square root of time / s$^{-1/2}$
923 K
973 K
1073 K
1023 K

Fig. 3

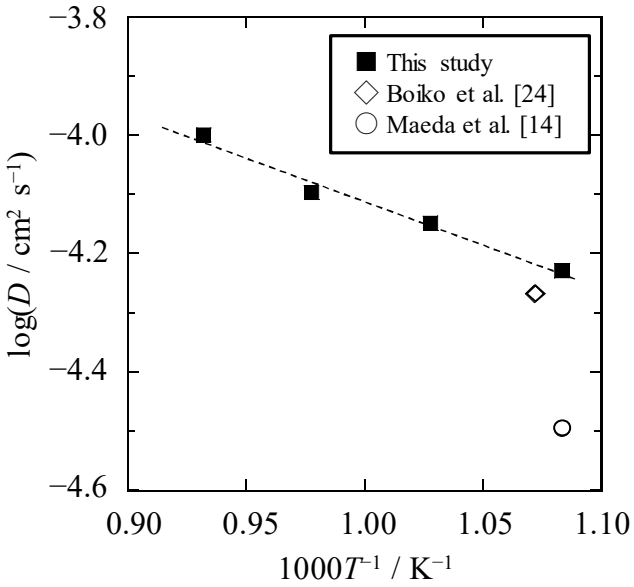
−3.8
−4.0
−4.2
−4.4
−4.6
log(D / cm² s⁻¹)
0.90
0.95
1.00
1.05
1.10
1000T⁻¹ / K⁻¹
This study
Boiko et al. [24]
Maeda et al. [14]

Fig. 4

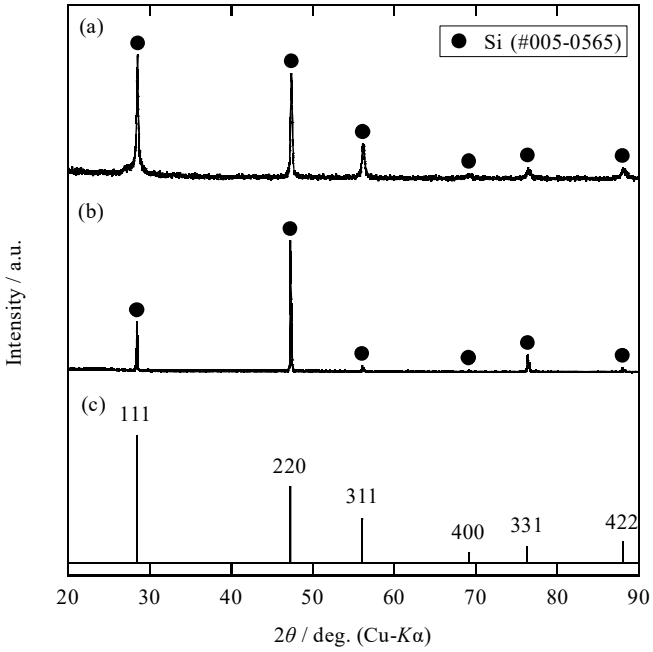
(a)
Si (#005-0565)
(b)
(c)
111
220
311
400
331
422
Intensity / a.u.
20
30
40
50
60
70
80
90
2θ / deg. (Cu-Kα)

Fig. 5

Fig. 6

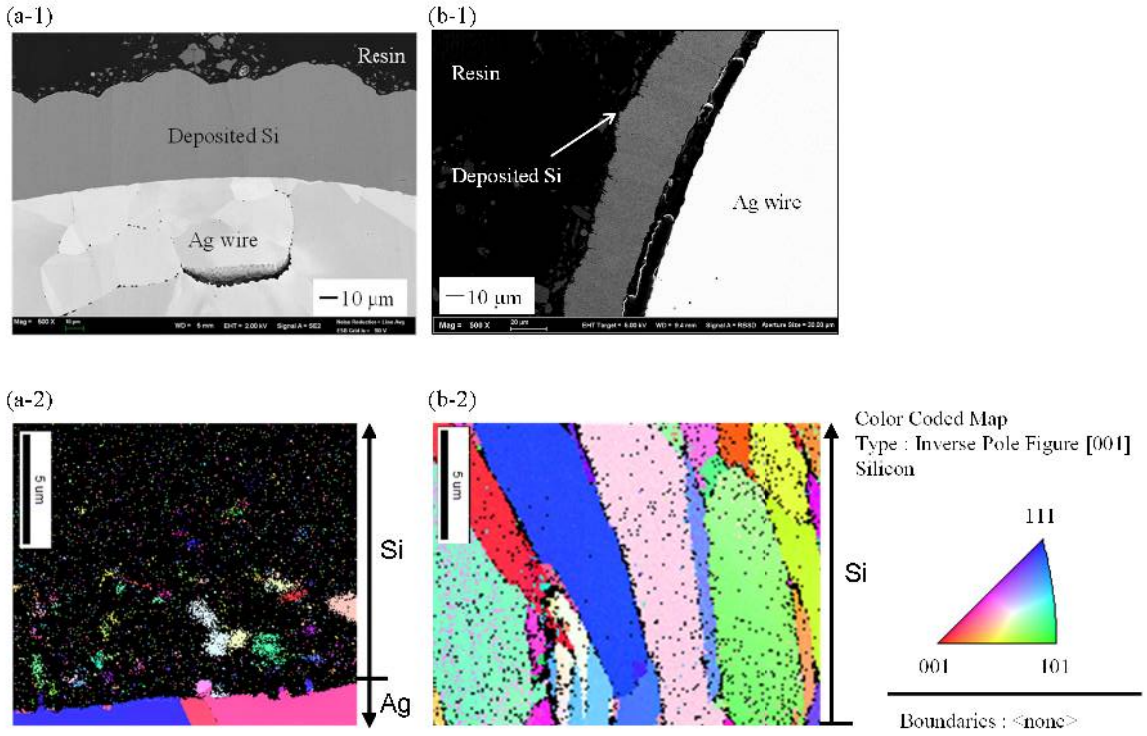
(a-1)
Resin
Deposited Si
Ag wire
10 μm
(b-1)
Resin
Deposited Si
Ag wire
10 μm
(a-2)
5 um
Si
Ag
(b-2)
5 um
Si
Color Coded Map
Type : Inverse Pole Figure [001]
Silicon
111
001
101
Boundaries : <none>

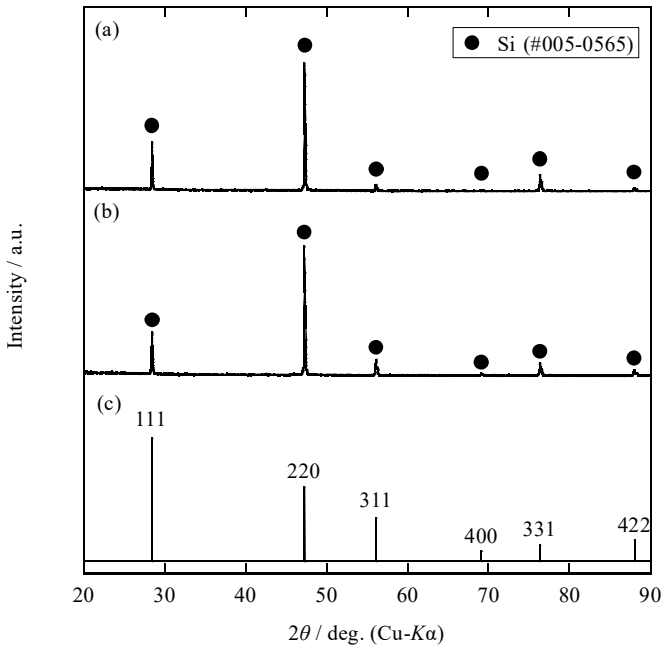
(a)
Si (#005-0565)
(b)
(c)
111
220
311
400
331
422
Intensity / a.u.
20
30
40
50
60
70
80
90
2θ / deg. (Cu-Kα)

Fig. 7

Fig. 8

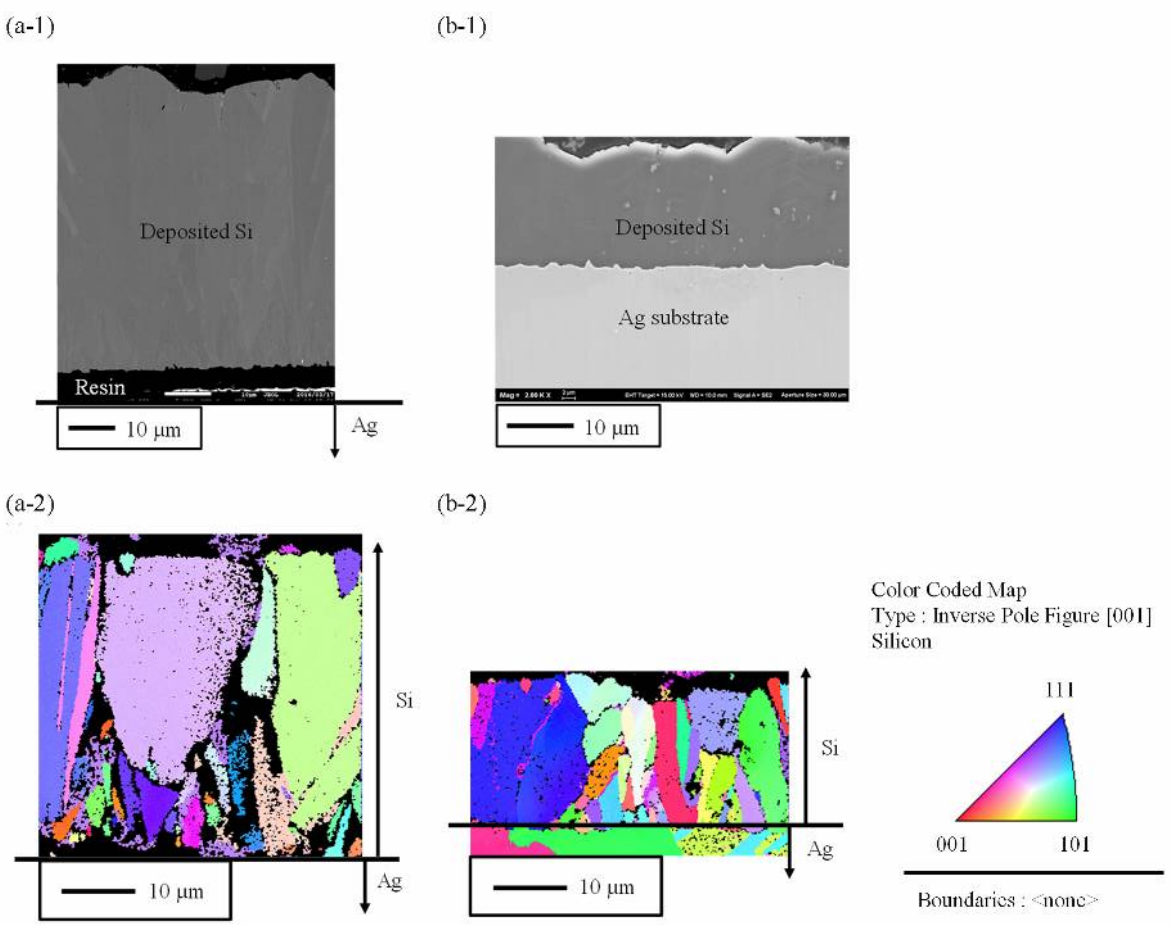
(a-1)
Deposited Si
Resin
10 μm
Ag
(b-1)
Deposited Si
Ag substrate
10 μm
(a-2)
Si
10 μm
Ag
(b-2)
Si
Ag
10 μm
Color Coded Map
Type : Inverse Pole Figure [001]
Silicon
111
001
101
Boundaries : <none>

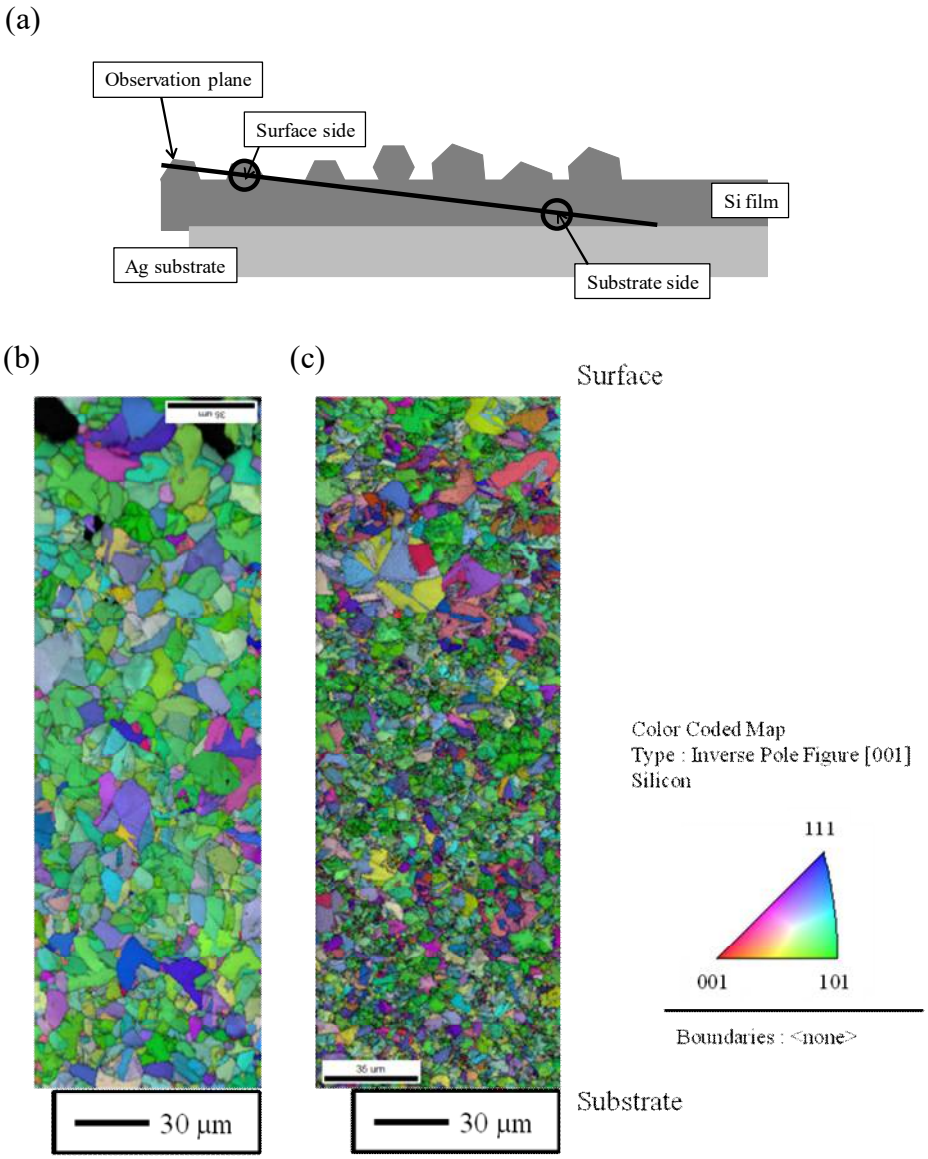
(a)
Observation plane
Surface side
Si film
Ag substrate
Substrate side
(b)
(c)
Surface
Color Coded Map
Type : Inverse Pole Figure [001]
Silicon
111
001
101
Boundaries : <none>
30 μm
30 μm
Substrate

Fig. 9

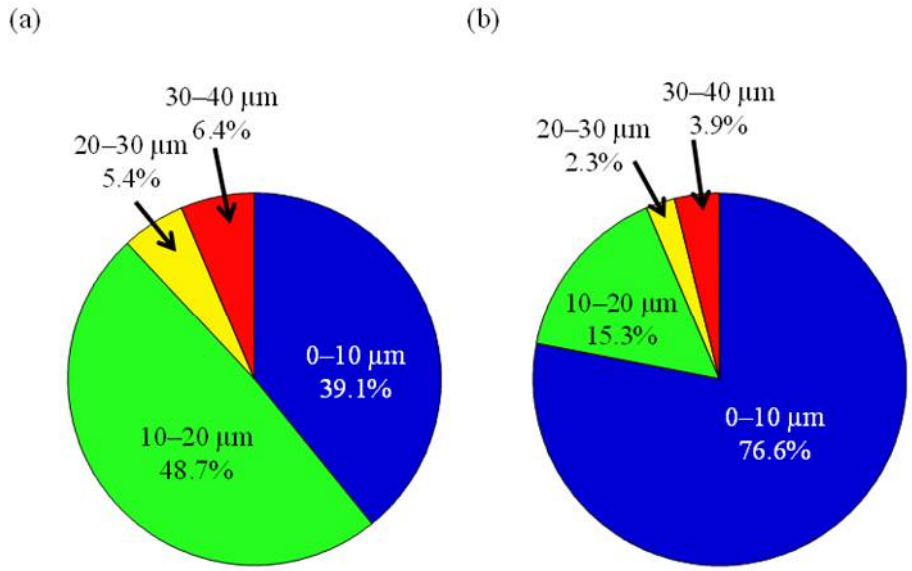
(a)
30–40 µm
6.4%
20–30 µm
5.4%
0–10 µm
39.1%
10–20 µm
48.7%
(b)
30–40 µm
3.9%
20–30 µm
2.3%
10–20 µm
15.3%
0–10 µm
76.6%

Fig. 10

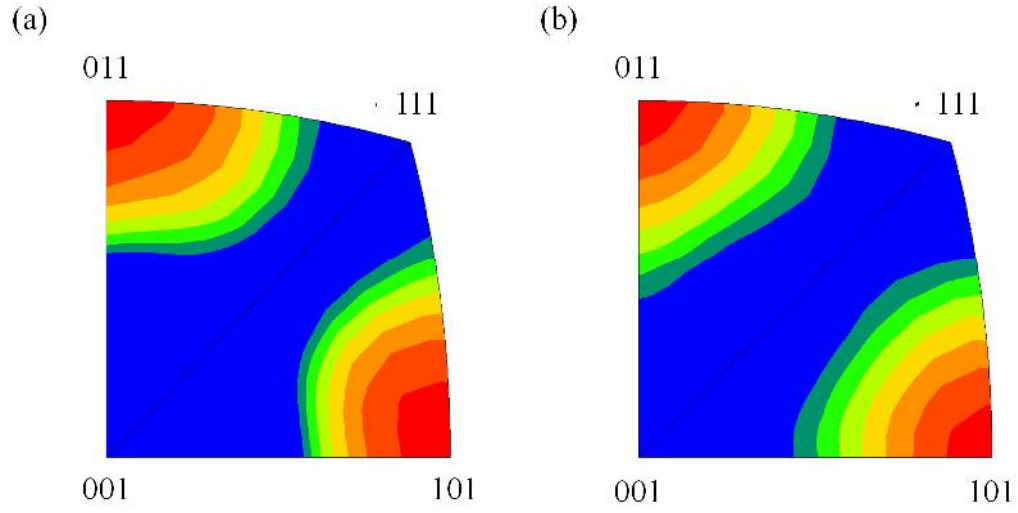

Fig. 11.